Self-similar nested sequences on a chaotic attractor for traveling-wave electrophoresis

Boyd F. Edwards

Department of Physics, West Virginia University, Morgantown, West Virginia 26506, USA

Oscillating electric potentials are applied to interdigitated arrays of cylindrical electrodes above and below a stationary conducting viscous fluid. The phases of these potentials are chosen to produce a longitudinal traveling wave that traps high-mobility ions and partially traps intermediate-mobility ions in periodic and narrowband chaotic attractors with average velocities that are commensurate with the wave speed. Stable periodic attractors have periods up to 101 times the wave period. Incommensurate broadband chaotic attractors are described by one-dimensional iterated contact-angle return maps, which feature self-similar nested sequences that converge geometrically at unstable trapped orbits. Sequences of singular angles and sequences of step transitions are characterized by distinct convergence factors. A criterion for allowed interelectrode orbits is developed. Experiments are suggested to evaluate the applicability of the theory to microfluidic separations.

I. INTRODUCTION

Since Edward Lorenz's 1963 discovery of aperiodic nonlinear behavior with sensitivity to initial conditions in a simple model of buoyancy-driven convection [1], such chaotic behavior has been identified in virtually every field of science and technology. The fascination of chaos is that deterministic systems of equations can produce inherently unpredictable behavior marked by the divergence of nearby phase-space trajectories.

While Lorenz investigated the time-dependent amplitudes of three modes that are fixed in space, recent interest in nonlinear dynamics has been drawn to spatial patterns that evolve with time. Examples include wave behavior in the photosensitive Belousov-Zhabotinsky chemical reaction with imposed spatiotemporal noise [2,3], wave mediated synchronization of coupled chemical oscillatory cells with randomly distributed frequencies [4], localized excitations in arrays of synchronized coupled laser oscillators [5], coupled arrays of forced, damped, nonlinear oscillators [6], and periodic pulling in light-emission fluctuations in neon glow discharges [7].

In this paper, we model the motion of ions of charge q, hydrodynamic radius r, and velocity $\mathbf{v}$ through a stationary electrically conducting fluid of viscosity η in response to a four-phase oscillating electric potential applied to periodic arrays of stationary cylindrical electrodes. In contrast with previous studies of oscillator synchronization [4–6,8], the potentials of our oscillators are external functions of time and the focus is on the dynamical response of ions to the resulting spatiotemporal forcing.

Our potentials are chosen to produce a longitudinal traveling wave that traps high-mobility ions, separating them from lower-mobility ions in a process called traveling-wave electrophoresis (TWE). We recently observed this phenomenon for a sandwich architecture in which a microfluidic channel is bounded above and below by electrode-bearing surfaces [9]. The purpose of the present paper is to investigate the associated nonlinear dynamical behavior in order to guide the design of new experiments.

Others have used interdigitated electrode arrays on a single surface to transport charged species via electrophoresis, imposing static perpendicular gravitational or electric fields to draw particles to the surface [10–12]. Our sandwich architecture precludes such fields by bounding a microfluidic channel by electrode-bearing surfaces above and below. Single-surface architectures can also transport charged particles via ac electro-osmotic pumping [13,14] or biased Brownian motion [15], and can transport neutral bioparticles via dielectrophoresis [16,17].

Our two-dimensional (2D) model employs a spatially periodic electrode pattern with four cylindrical electrodes per wavelength (Fig. 1) that create and sustain a 2D traveling wave, consistent with the Nyquist-Shannon requirement of more than two electrodes per wavelength [18,19]. The four electrodes are held at oscillating potentials $\Phi_0(t)$, $\Phi_1(t)$, $\Phi_2(t)$, and $\Phi_3(t)$ that are synchronized so that each electrode leads its neighbor to the right in phase by $\pi/2$ according to

$$\Phi_i(t) = \phi_0 \sin(kx_i - \omega t), \tag{1}$$

where ϕ_0 is the potential amplitude, $k = 2\pi/\lambda$ is the wave number, $x_i = i\lambda/4$ denotes the axial position of electrode i,
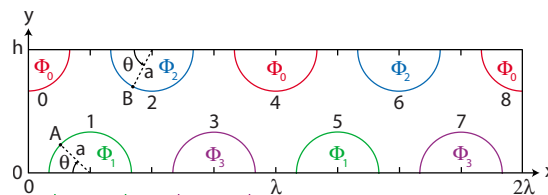
FIG. 1. (Color online) Channel geometry and periodic four-electrode pattern of wavelength λ considered herein, a pattern replicated indefinitely in the $\pm x$ directions. Shown are two replicates of this pattern including electrode numbers $i = 0, 1, 2, \dots, 8$ located at $x_i = i\lambda/4$. Electrodes are treated as impenetrable conducting half-cylinders of radius $a \ll \lambda$ ($a \approx \lambda$ in the figure for clarity) with axes perpendicular to the plane of the figure. Oscillating electric potentials $\Phi_0(t)$, $\Phi_1(t)$, $\Phi_2(t)$, and $\Phi_3(t)$ given by Eq. (1) are applied to the electrodes and are synchronized so that each electrode leads its neighbor to the right in phase by $\pi/2$, producing a wave propagating to the right that traps high-mobility ions. Positions on electrode surfaces (points A and B) are denoted by contact angles θ measured in radians and satisfying $0 \le \theta \le \pi$, with $\theta = 0$, $\pi/2$, and π corresponding to the leftmost, middle, and rightmost contact points.

and $\omega = 2\pi/\tau$ is the angular frequency of the oscillations. Equation (1) gives the discrete potentials of the electrodes that are arranged in the 2D pattern shown in Fig. 1. As will be discussed below, these potentials serve as boundary conditions of Laplace's equation, which determines the potential throughout the channel.

We include only the electric force $\mathbf{F}_E = q\mathbf{E}$ and the Stokes drag force $\mathbf{F}_D = -6\pi\eta r\mathbf{v}$ on the ions, ignoring magnetic and gravitational fields, molecular diffusion, and ionic inertia. Accordingly setting $\mathbf{F}_E + \mathbf{F}_D = 0$ yields the electrophoretic velocity

$$\mathbf{v} = \mu\mathbf{E} \qquad (2)$$

and mobility $\mu = q/6\pi\eta r$, where $\mathbf{E}(x,y,t) = -\nabla\phi(x,y,t)$ is the 2D time-dependent electric field that results from the applied electrode potentials. Equation (2) differs from the Maxwellian distribution of electron velocities pertinent to particle trapping by longitudinal plasma waves and Langmuir waves [20–22].

We define the responsiveness

$$R = \frac{\mu E_0}{c} \qquad (3)$$

of an ion to the wave as the dimensionless ratio of a characteristic electrophoretic velocity μE_0 to the wave speed $c = \omega/k$, where $E_0 = k\phi_0$ is a characteristic electric field. Here, $q > 0$ and $R > 0$ for cations and $q < 0$ and $R < 0$ for anions.

Combining Eq. (2) with $\mathbf{v} = \dot{x}$ and specifying the electric potential $\phi(x,y,t)$ yields a 2D nonlinear nonautonomous system of ordinary differential equations

$$\dot{x} = f(x,y,t) \qquad (4)$$

$$\dot{y} = g(x,y,t), \qquad (5)$$

with functions

$$f(x,y,t) = -\mu\,\partial\phi/\partial x \qquad (6)$$

$$g(x,y,t) = -\mu\,\partial\phi/\partial y \qquad (7)$$

that depend explicitly on time. Accordingly, this system has a three-dimensional (3D) phase space, the minimum dimensionality needed for chaos [23]. Previous studies of 2D nonautonomous systems [24] exclude impenetrable barriers such as our electrodes, whose oscillating potentials determine the potential $\phi(x,y,t)$ within the microchannel.

Periodically forced oscillators, which have received considerable attention [8], obey equations of the general form of Eqs. (4) and (5), but have functions f and g that exclude Eqs. (6) and (7), reflecting fundamental physical differences. A periodically forced oscillator must reconcile its internal rhythm against the amplitude and frequency of some external forcing. Our ions have no internal rhythm of their own and are subject only to external forcing, which entirely determines their dynamics. Forced oscillators obey

$$\ddot{x} + \omega_0^2 x = h(x,\dot{x},t), \qquad (8)$$

where $h(x,\dot{x},t)$ is generally some nonlinear function that is periodic in time, and where inertia supplies the second-order
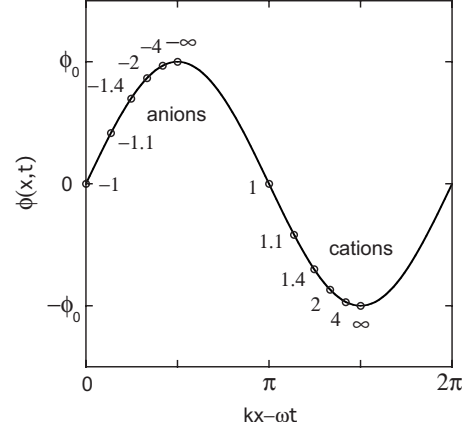
FIG. 2. Steady-state phases from Eq. (11) (circles) for ions trapped by a 1D electric potential wave from Eq. (9) (solid trace) traveling through a stationary viscous fluid. Trapped cations with dimensionless mobilities $R \geq 1$ (numerical values accompanying cation phases) travel on the trailing sides of potential wells, with lower-mobility cations requiring stronger electric fields to overcome Stokes drag. Trapped anions with $R \leq -1$ travel on the trailing sides of peaks. Ions with $|R| < 1$ are not trapped by the wave, but execute periodic oscillations at a frequency given by Eq. (12).

term. Particle inertia is negligible in our system. For forced oscillators, Eqs. (4) and (5) can be recast as Eq. (8) by setting $f(x,y,t) = y$ and $g(x,y,t) = h(x,y,t) - \omega_0^2 x$. Our system cannot be similarly recast because Eq. (6) is a specified periodic function of space and time.

II. 1D MODEL

Insight into wave electrophoresis is supplied by a one-dimensional (1D) model [25,26] with a specified electric potential

$$\phi(x,t) = \phi_0 \sin(kx - \omega t) \qquad (9)$$

and with no electrodes. This potential mimics the applied electrode potentials of Eq. (1) and corresponds to a longitudinal electric field

$$\mathbf{E}(x,t) = -E_0\hat{x}\cos(kx - \omega t). \qquad (10)$$

For $|R| \geq 1$, after the decay of transients, this model predicts a constant velocity $v_x = c$ for trapped cations and anions, with cations traveling within potential wells and anions within peaks, and both traveling in the direction of wave propagation. The steady-state phase $\delta = kx - \omega t$ of trapped ions satisfies

$$\cos\delta = -1/R. \qquad (11)$$

Hence, high-mobility cations with $R \to \infty$ are trapped at potential minima while threshold-mobility cations with $R = 1$ are trapped at electric-field maxima. High-mobility anions with $R \to -\infty$ are trapped at potential maxima while threshold-mobility anions with $R = -1$ are trapped at electric-field minima (Fig. 2). High-mobility ions cannot exceed the wave speed because $\mathbf{F}_E$ drives ions toward extrema in the potential, where $\mathbf{F}_E$ vanishes. The larger the mobility, the

nearer to these extrema that ions reside in steady state.

For $|R| < 1$, ions are insufficiently mobile to keep pace with the wave. After decay of transients, these ions experience regular longitudinal oscillations of angular "lag" frequency

$$\Omega = \omega(1 - R^2)^{1/2} \tag{12}$$

and make net forward progress with average velocity [25]

$$\frac{\bar{v}_x}{c} = 1 - (1 - R^2)^{1/2}. \tag{13}$$

During each oscillation, an ion fails to catch a passing wave and lags one cycle behind the wave, like a surfer failing to catch a passing ocean wave. For $|R| \ll 1$, ions experience one lag cycle for each wave cycle ($\Omega \to \omega$) and make only very slow net forward progress ($\bar{v}_x/c \to R^2/2$). For $|R| \to 1$, ions have long lag cycles ($\Omega \ll \omega$) and net velocities that approach the wave speed ($\bar{v}_x \to c$). This limit anticipates the time-independent results $\Omega = 0$ and $v_x = c$ for $|R| \geq 1$.

III. 2D MODEL

Viscous damping would quickly attenuate a wavelike equation (9) unless some means of sustaining it is provided. For this purpose, we employ a spatially periodic electrode pattern with four conducting cylindrical electrodes per wavelength (Fig. 1) to create and sustain a 2D wave that mimics the 1D wave of Eq. (9), with four-electrode potentials $\Phi_0(t)$, $\Phi_1(t)$, $\Phi_2(t)$, and $\Phi_3(t)$ given by Eq. (1), which demands that $\Phi_2 = -\Phi_0$ and $\Phi_3 = -\Phi_1$.

We assume an electrically neutral bulk solution, in contrast with the 1D model which requires non-neutrality. We treat the time required for charges to redistribute within the electrically conducting buffer solution as small compared with τ, the period of the oscillating potentials that drive this charge redistribution. In this electrostatic approximation, the 2D electric potential $\phi(x,y,t)$ within the solution must satisfy Laplace's equation,

$$\nabla^2 \phi = 0. \tag{14}$$

This potential must also match the four time-dependent potentials at the conducting electrode surfaces and must ensure vanishing normal electric field $E_y = -\partial\phi/\partial y = 0$ at the insulating boundaries at $y = 0$ and $y = h$.

To investigate the role of geometry on the dynamics, we define the aspect ratio $\Gamma = \lambda/h$ as the ratio of the electrode wavelength λ to the microchannel height h.

Long electrodes facilitate simple closed-form mathematical representations of the electric potential in the microchannel. The potential produced by two long cylindrical electrodes of radius a separated by a distance of $\lambda/2$ and held at potentials Φ_0 and $\Phi_2 = -\Phi_0$ is

$$\phi = \Phi_0 \frac{\ln(r_2/r_0)}{\ln(\lambda/2a)}, \tag{15}$$

where r_0 is the distance between one electrode center and the point at which the potential is being evaluated, and r_2 is the distance from this point to the other electrode center. Equa-

tion (15) satisfies Eq. (14) and the boundary conditions $\phi|_{r_0=a} = \Phi_0$ and $\phi|_{r_2=a} = \Phi_2 = -\Phi_0$ when $a \ll \lambda$, and follows from the potential of two parallel infinite line charges with opposite uniform linear charge densities [27]. The potential produced by electrodes held at potentials Φ_1 and $\Phi_3 = -\Phi_1$ is similar,

$$\phi = \Phi_1 \frac{\ln(r_3/r_1)}{\ln(\lambda/2a)}. \tag{16}$$

We now employ a linear superposition of Eqs. (15) and (16) to write the potential at a 2D position $\mathbf{r} = (x,y)$ in the channel and at time t,

$$\phi(\mathbf{r},t) = \frac{\Phi_0(t)}{\ln(\lambda/2a)} \sum_{l,m=-\infty}^{\infty} \ln\frac{|\mathbf{r} - \mathbf{r}_2^{(l,m)}|}{|\mathbf{r} - \mathbf{r}_0^{(l,m)}|}$$
$$+ \frac{\Phi_1(t)}{\ln(\lambda/2a)} \sum_{l,m=-\infty}^{\infty} \ln\frac{|\mathbf{r} - \mathbf{r}_3^{(l,m)}|}{|\mathbf{r} - \mathbf{r}_1^{(l,m)}|}, \tag{17}$$

where

$$\mathbf{r}_0^{(l,m)} = (l\lambda, h + 2mh) \tag{18a}$$

$$\mathbf{r}_1^{(l,m)} = (\lambda/4 + l\lambda, 2mh) \tag{18b}$$

$$\mathbf{r}_2^{(l,m)} = (\lambda/2 + l\lambda, h + 2mh) \tag{18c}$$

$$\mathbf{r}_3^{(l,m)} = (3\lambda/4 + l\lambda, 2mh) \tag{18d}$$

are the position vectors of the electrode centers shown in Fig. 3. The value $m = 0$ corresponds to the physical microchannel electrodes, whose $l = 0$ and $l = 1$ replicates are shown in Fig. 1. The replicates for $m = \pm 1, \pm 2, \ldots$ lie outside of the physical domain $0 \leq y \leq h$ of the microchannel and correspond to image charges used to ensure vanishing normal electric field at $y = 0$ and $y = h$.

Evaluating the potential $\phi(\mathbf{r},t)$ and the electric field $\mathbf{E} = -\boldsymbol{\nabla}\phi$ using Eq. (17) poses a challenge because the terms in the infinite sums depend on the electrode distances as $\ln r$ and $1/r$, respectively. Accordingly, straightforward truncations of these sums violate the periodicity property $\mathbf{E}(x + \lambda, y) = \mathbf{E}(x,y)$, the symmetry property $\mathbf{E}(x + \lambda/2, y) = -\mathbf{E}(x,y)$, and the boundary conditions $E_y(0,y) = 0$ and $E_y(h,y) = 0$. To avoid these violations and to preserve overall electrical neutrality, we use these periodicity and symmetry properties to translate x onto the interval $0 \leq x < \lambda/2$ and truncate the infinite sums according to

$$\phi(\mathbf{r},t) = \frac{\Phi_0(t)}{\ln(\lambda/2a)} \sum_{l=-L}^{L} \sum_{m=-M}^{M} a_m \ln\frac{|\mathbf{r} - \mathbf{r}_2^{(l,m)}|^{c_l}}{|\mathbf{r} - \mathbf{r}_0^{(l,m)}|^{b_l}}$$
$$+ \frac{\Phi_1(t)}{\ln(\lambda/2a)} \sum_{l=-L}^{L} \sum_{m=-M}^{M} d_m \ln\frac{|\mathbf{r} - \mathbf{r}_3^{(l,m)}|^{f_l}}{|\mathbf{r} - \mathbf{r}_1^{(l,m)}|^{e_l}}, \tag{19}$$

adjusting the weights of the perimeter terms, that is, terms with $l = \pm L$ and $m = \pm M$, by introducing coefficients satisfying $a_m = b_l = c_l = d_m = e_l = f_l = 1$ for all l and m except

$$a_M = y/h \tag{20a}$$
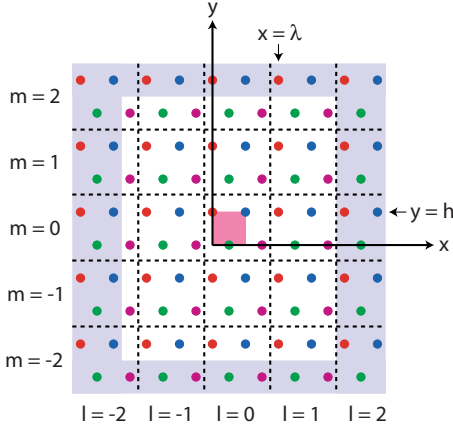
FIG. 3. (Color online) Periodic electrode pattern used in computing $\phi(x,y,t)$ from Eq. (19), with electrodes held at potentials Φ_0, Φ_1, Φ_2, and Φ_3 located respectively at positions $\mathbf{r}_0^{(l,m)}$, $\mathbf{r}_1^{(l,m)}$, $\mathbf{r}_2^{(l,m)}$, and $\mathbf{r}_3^{(l,m)}$ from Eq. (18). Dashed lines separate replicates of this pattern identified by their values of l and m. Replicates for $m=0$ correspond to the physical electrode pattern of the channel (Fig. 1). Replicates for $m \neq 0$ correspond to image charges needed to ensure $\partial\phi/\partial y = 0$ at the channel boundaries $y=0$ and $y=h$. The diagram applies to calculations of $\phi(x,y,t)$ within the central computational area (shaded) defined by $0 \leq x < \lambda/2$ and $0 \leq y < h$, and for the truncations $L = M = 2$. Contributions of the peripheral electrodes (also shaded) with $l = \pm L$ and $m = \pm M$ receive reduced weights according to Eq. (20) in order to satisfy the boundary conditions and to ensure symmetry and continuity, while the contributions of the remaining interior electrodes are included fully in the calculations.

$$b_L = \begin{cases} 2x/\lambda + 1/2, & 0 \leq x < \lambda/4 \\ 1, & \lambda/4 \leq x < \lambda/2 \end{cases} \quad (20\mathrm{b})$$

$$b_{-L} = 1 - b_L \quad (20\mathrm{c})$$

$$c_L = \begin{cases} 0, & 0 \leq x < \lambda/4 \\ 2x/\lambda - 1/2, & \lambda/4 \leq x < \lambda/2 \end{cases} \quad (20\mathrm{d})$$

$$c_{-L} = 1 - c_L \quad (20\mathrm{e})$$

$$d_{-M} = 1 - a_M \quad (20\mathrm{f})$$

$$e_L = 2x/\lambda \quad (20\mathrm{g})$$

$$e_{-L} = 1 - e_L \quad (20\mathrm{h})$$

$$f_L = 0 \quad (20\mathrm{i})$$

$$f_{-L} = 1. \quad (20\mathrm{j})$$

These relationships emphasize the $l = -L$ contributions for $x \approx 0$ and the $l = +L$ contributions for $x \approx \lambda/2$ in order to simulate an unbounded periodic system. The values $L = 60$ and $M = 2$ ensure electric fields that are accurate to within 1%, as verified by comparing with solutions with larger L. For $L = 60$, we computed the numerical Laplacian of Eq. (19) for various values of M and found that $M = 2$ best satisfies

Laplace's equation, giving $|\nabla^2\phi| \leq 0.01$ V/μ m^2 over the entire domain for $\phi_0 = 0.5$ V, $\lambda = 80$ μm, $h = 15$ μm, and $a = 1$ μm.

We have written a computer code to simulate the motion of ions subject to the traveling-wave potential given by Eq. (19). The code integrates Eqs. (4) and (5) using a fifth-order Runge-Kutta-Fehlberg method with adaptive stepsize control [28], using about 200 electric-field evaluations to integrate an ionic path between adjacent electrodes, and predicting electrode contact angles that are accurate to within 1%. The convergence of the code was verified by decreasing the average stepsize and by comparing with the results of a simpler, but much slower, forward Euler integration with fixed step size that employs as many as 4000 electric-field evaluations between electrodes. We also verified the code by using it to recover Eq. (13) of the 1D model.

We follow trajectories for a time $\Delta t = 2000\tau$ in order to determine the average axial velocity

$$\bar{v}_x = \frac{x_2 - x_1}{\Delta t}, \quad (21)$$

where x_1 and x_2 are the initial and final positions of the ion along the x axis.

IV. ORBIT CONDITION

The phase relationships between the electrode potentials restrict the allowed interelectrode orbits. Ions that are immobilized electrostatically at electrode surfaces depart at (for $\theta = 0$) or near (for $\theta \neq 0$) the time at which the sign of the electrode potential changes to the sign of the charge of the immobilized ion. For electrode i, this time is $t_j = j\tau/4$, with integer $j = i + 4m$ for anions and integer $j = i + 4m + 2$ for cations, and with integer m. Accordingly, the axial ion displacement Δi (in quarter wavelengths) between successive electrode departures and the corresponding elapsed time Δj (in quarter periods) satisfy $\Delta j = \Delta i + 4m$, valid for both cations and anions. The average axial velocity between departures must therefore satisfy the interelectrode orbit condition

$$\frac{\bar{v}_x}{c} = \frac{\Delta i}{\Delta j} = \frac{\Delta i}{\Delta i + 4m}, \quad (22)$$

where $m \geq 0$ is the number of lag cycles during the elapsed time $\Delta t = \Delta j \tau/4$. The corresponding lag frequency is

$$\Omega = \frac{4m}{\Delta i + 4m}\omega. \quad (23)$$

Interelectrode orbits must satisfy Eq. (22), which contains both velocity and orbital information. While the dimensionless interelectrode velocity is determined solely by the ratio $\Delta i/\Delta j$, the numerator and denominator of this ratio also carry information about the orbit. We therefore characterize orbits by an integer ratio of the form $\Delta i : \Delta j$. A 2:2 orbit is distinct from a 1:1 orbit even though they have the same velocity, $\bar{v}_x = c$. A 2:2 orbit takes two quarter periods to travel between electrodes on the same side of the channel, electrodes that are separated axially by two quarter wavelengths (electrodes 4 and 6 in Fig. 1, for example). In contrast, a 1:1
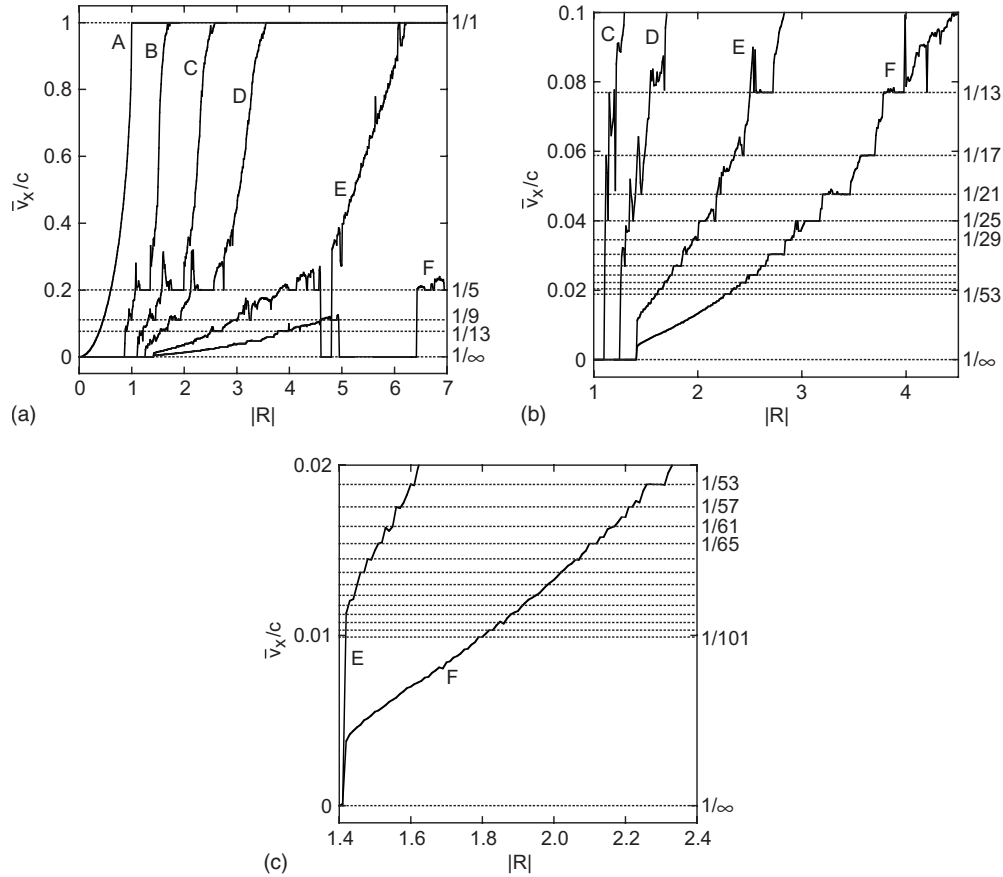
FIG. 4. (a) Ratio of the steady-state average axial ion velocity $\bar{v}_x$ to the wave speed c vs the responsiveness R of Eq. (3). Shown are results for the 1D model from Eq. (13) (trace A) and numerical results for the 2D model for electrode pattern wavelength $\lambda = 80$ μm, electrode radius $a = 1$ μm, and channel heights $h = 10$, 15, 20, 30, and 40 μm giving aspect ratios $\Gamma = \lambda/h = 8$, 5.3, 4, 2.7, and 2 (traces B, C, D, E, and F). Traces for the 2D model feature commensurate velocity plateaus satisfying Eq. (22) (horizontal dashed traces and integer ratios). Frames (b) and (c) show small-velocity detail.

orbit takes one quarter period to travel between electrodes on opposite sides of the channel, electrodes that are separated axially by one quarter wavelength (electrodes 4 and 5 in Fig. 1, for example).

V. VELOCITIES AND PERIODIC ATTRACTORS

Results for $\bar{v}_x$ for the 2D model show structure that is not seen in the 1D model. Equation (13) of the 1D model predicts a $\bar{v}_x$ that rises monotonically with increasing $|R| \gtrsim 0$ until it reaches $\bar{v}_x = c$ at the trapping threshold $R_t = 1$, above which $\bar{v}_x = c$ (Fig. 4, trace A). The 2D model (Fig. 4, traces B-F) features larger trapping thresholds R_t reflecting incomplete penetration of the potential into the interior of the channel, nonzero localization thresholds R_l below which electrodes completely localize low-mobility ions ($\bar{v}_x = 0$), and plateaus with commensurate velocities $\bar{v}_x/c = 1, 1/5, 1/9, \ldots$ satisfying Eq. (22) with $\Delta i = 1$ and $m = 0, 1, 2, \ldots, 25$. Each trace in Fig. 4 satisfies $\bar{v}_x = 0$ for $R < R_l$ and $\bar{v}_x = c$ for $R > R_t$, with localization and trapping thresholds R_l and R_t specific to each trace. For the 1D model, $R_l = 0$ and $R_t = 1$.

The velocity plateaus are associated with periodic attractors. For $\Gamma = 4$ (Fig. 4, trace D), trajectories for cations and anions with arbitrary initial positions converge to the attrac-

tors shown in Fig. 5. Trapped ions of velocity 1 choose between attractors restricted to the upper and lower electrodes, both employing 2:2 orbits. Ions of velocity 1/5 and 1/9 possess attractors respectively involving 1:5 and 1:9 orbits, orbits that connect the upper and lower electrodes. Localized ions for $R < R_l$ employ 0:4 orbits (not shown) that oscillate in the $\pm x$ direction at $y = 0$ or $y = h$ and contact the right sides of electrodes (at $\theta = \pi$) once per period. Orbits are replicated again and again as the ion moves along the channel in the $+x$ direction, as shown in Fig. 5. Lag cycles for the velocity-1/5 and 1/9 attractors involve temporary reversals of the direction of motion that result when the traveling wave passes by an ion and temporarily pushes it in the $-x$ direction, like a surfer failing to catch a passing ocean wave. Sudden changes in orbital direction result when electrode voltages change sign, switching from attracting to repelling.

Attractors with larger periods and smaller velocities involve combinations of orbits, as shown for $\Gamma = 2$ in Fig. 6 (see Fig. 4, trace F). The velocity-1/13 attractor involves 0:4, 2:2, and -1:7 orbits for each cycle of the attractor, repeated over and over again. Each cycle advances the ion forward by one electrode. Labeled in Fig. 6(a) are the orbits associated with the cycle that begins at electrode 0 and ends at electrode 1, making a stop at the intermediate electrode 2 along the
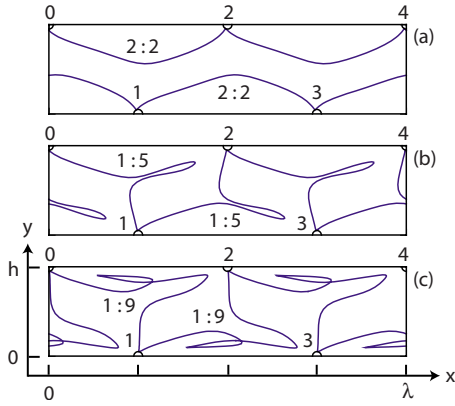
FIG. 5. (Color online) Periodic attractors associated with velocity plateaus of Fig. 4, trace D, for aspect ratio $\Gamma = \lambda/h = 4$. Each frame shows one wavelength of the electrode pattern of Fig. 1, with numbered electrodes of radius $a = \lambda/80$ shown to scale as small semicircles. Shown are steady-state trajectories of ions moving through a stationary viscous solution in response to the 2D traveling-wave potential of Eq. (19) after the decay of transients. Trajectories that disappear through the right side of the frames reappear on the left. (a) Two attractors of velocity 1 for $R = 3.6$ involving successive identical 2:2 interelectrode orbits, one attractor involving the upper electrodes 0,2,4,... and the other involving the lower electrodes 1,3,5,.... (b) Attractor of velocity 1/5 for $R = 2.5$ involving 1:5 orbits, with one lag cycle per orbit [$m = 1$ in Eq. (22)] during which the ion lags one cycle behind the traveling wave. (c) Attractor of velocity 1/9 for $R = 1.92$ involving 1:9 orbits with two lag cycles each ($m = 2$).

way. The second cycle takes the ion from electrode 1 to electrode 2, making a stop at the intermediate electrode 3 along the way, etc. Because the velocity is the net displacement divided by the elapsed time, it is given by the Farey sum of the orbits,

$$\frac{0}{4} \oplus \frac{2}{2} \oplus \frac{-1}{7} = \frac{1}{13}, \tag{24}$$

where Farey addition is defined as [29]

$$\frac{a}{b} \oplus \frac{c}{d} \equiv \frac{a+b}{c+d}. \tag{25}$$

Each cycle of the velocity 1/53 attractor [Fig. 6(b)] involves 0:4 and 1:49 orbits and avoids the intermediate electrode. Each cycle of the 1/101 attractor [Fig. 6(c)] involves 0:4, 0:4, 2:54, and −1:39 orbits and does contact the intermediate electrode. It is easy to show that Farey sums of orbits obey the interelectrode orbit condition [Eq. (22)] as long as each term in the sum obeys this condition. Accordingly, it is no surprise that attractors that involve combinations of allowed orbits have velocities (such as 1/13, 1/53, and 1/101) that obey Eq. (22).

Small aspect-ratio geometries $\Gamma = \lambda/h = 2$ and 2.7 (traces F and E in Fig. 4) suffer from zero-velocity windows ($5 < |R| < 6.4$ for trace F, for example) and larger partial-trapping ranges $R_t - R_l$, which render them less suitable for experimental separations than higher-aspect-ratio geometries. These zero-velocity windows represent localized modes
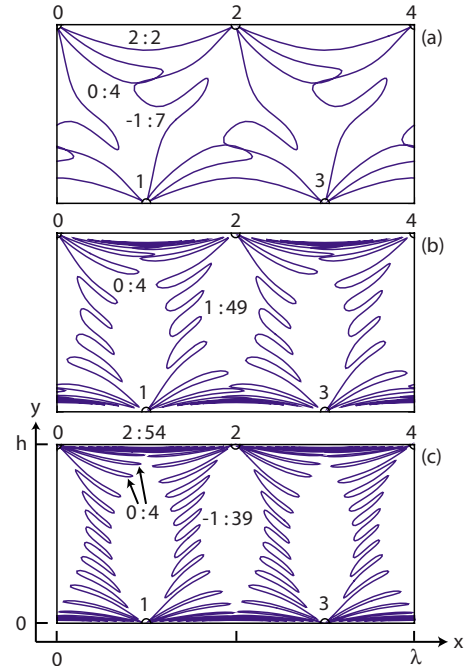
FIG. 6. (Color online) Periodic attractors associated with velocity plateaus of Fig. 4, trace F, for aspect ratio $\Gamma = 2$ after the manner of Fig. 5, with velocities 1/13, 1/53, and 1/101 for $R = 3.94$ (a), 2.28 (b), and 1.80 (c), respectively. Ion trajectories beginning at arbitrary initial positions quickly relax to these highly stable attractors.

which are sometimes barely stable to small perturbations.

The remainder of this paper is devoted to the detailed investigation of nonperiodic behavior for $\Gamma = 4$ (trace D in Fig. 4), a geometry that is suitable for experimental separations and that features three velocity plateaus: 1/5, 1/9, and 1/13.

VI. NARROWBAND CHAOTIC ATTRACTORS

Commensurate velocity plateaus support both periodic attractors and narrowband chaotic attractors. Figure 7, trace A, shows the velocity data for $\Gamma = 4$ from trace D of Fig. 4, together with steady-state values of the electrode contact angle θ encountered for simulations at fixed R after the decay of transients (scattered points and traces, B). This contact angle is measured in radians and is defined in Fig. 1, with $\theta = 0$, $\theta = \pi/2$, and $\theta = \pi$, respectively, representing the leftmost contact point, the midpoint, and the rightmost contact point on an electrode. At a particular value of R in Fig. 7, scattered values of the contact angle indicate a chaotic attractor, while one or more isolated values indicate a periodic attractor.

Commensurate velocity plateaus yield period-doubling cascades to narrowband chaos, cascades that are driven by translational symmetry-breaking transitions. Details of the velocity 1/5 plateau of Fig. 4 are shown in Fig. 8, which features a discontinuity in the steady-state contact angle at $R = 2.35$ (B) that corresponds to a glide-reflection symmetry-breaking transition. For $2.35 < R \leq 2.56$, the periodic attractor $y(x)$ obeys the quarter-wave glide-reflection symmetry
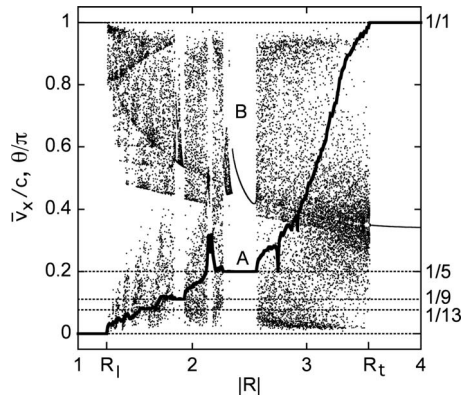
FIG. 7. Details of $\bar{v}_x/c$ vs. R for aspect ratio $\Gamma=4$ (heavy trace A, corresponding to trace D in Fig. 4), with localization and trapping thresholds $R_l=1.260$ and $R_t=3.554$. Also shown (b) are steady-state values of the electrode contact angle θ encountered for simulations at fixed R. Chaotic attractors (at $R=3.2$, for example) feature scattered random values of θ whose specific positions vary from simulation to simulation. Periodic attractors (at $R=2.4$, for example) feature one or more isolated values. Dashed lines identify commensurate velocity plateaus with $\bar{v}_x/c=1/5$, 1/9, and 1/13.

$y(x)=h-y(x+\lambda/4)$ and the translational symmetries $y(x)=y(x+2^{l-1}\lambda)$ for $l=0,1,\ldots,\infty$, employing four identical 1:5 orbits per wavelength as seen in Fig. 5(b). For $2.347<R\leq 2.35$, the attractor breaks the quarter-wave symmetry but obeys the half-wave ($l=0$) and higher translational symmetries, employing two identical 2:10 orbits per wavelength [Fig. 9(a), solid trace]. This attractor serves as the period-1 state for a period-doubling cascade. The period-2 attractor at $2.337<R\leq 2.347$ breaks the half-wave symmetry but obeys the whole-wave ($l=1$) and higher symmetries, alternating between two distinct 2:10 orbits with slightly different contact angles [Fig. 9(b), dashed trace]. In general, period-2^l attractors involve 2^l distinct 2:10 orbits, each with a different contact angle, and obey translational symmetries of order l and

higher. This period-doubling cascade converges at an accumulation point $R=2.334$ and appears in Fig. 8(b) as a bifurcation diagram that is similar to the familiar period-doubling bifurcation diagram for the logistic map [30,31]. Our simulations resolve period-1, 2, 4, 8, and 16 attractors.

The outcome of the period-doubling cascade is a velocity-1/5 narrowband chaotic attractor employing an infinite number of distinct 2:10 orbits as shown in Fig. 9(b) for $R=2.33$. Each orbit begins and ends at a different contact angle, with contact angles being restricted to a narrow range $0.449\pi<\theta<0.494\pi$ near the electrode midpoint. This range is evident in Fig. 8(b) (at $R=2.33$). On this narrowband chaotic attractor, the average velocity is commensurate with the wave speed ($\bar{v}_x/c=1/5$) because the attractor employs only 2:10 orbits, each of which has velocity 1/5.

The relationship between successive contact angles gives useful attractor information. We denote θ_n as the contact angle for the nth electrode contact, for $n=1,2,3,\ldots$, and consider return maps of θ_{n+1} as a function of θ_n after the decay of transients. Figure 10(a) shows attractors for four different values of R. The period-1 attractor is a single fixed point (circle) that lies on the line $\theta_{n+1}=\theta_n$ (dashed), reflecting that 2:10 orbits on this attractor are all identical, contacting electrodes successively at the same angle [Fig. 9(a), solid trace]. The two points on the period-2 attractor (squares) give the two values of θ that are visited alternately by this attractor [Fig. 9(a), dashed trace]. The four points on the period-4 attractor (triangles) are visited once each per cycle. The solid trace shows the continuous range of angles $0.449\pi<\theta<0.494\pi$ that are visited by the narrowband chaotic attractor [Fig. 9(b)]. All four attractors involve only 2:10 orbits and have velocity 1/5.

Details of the velocity 1/9 plateau of Fig. 4 are shown in Fig. 11, which shows a period-doubling cascade and a period-4 attractor flanked by period-2 attractors.

VII. BROADBAND CHAOTIC ATTRACTORS

This section is devoted entirely to the study of the structure of one broadband attractor, at $R=3.2$, which turns out to
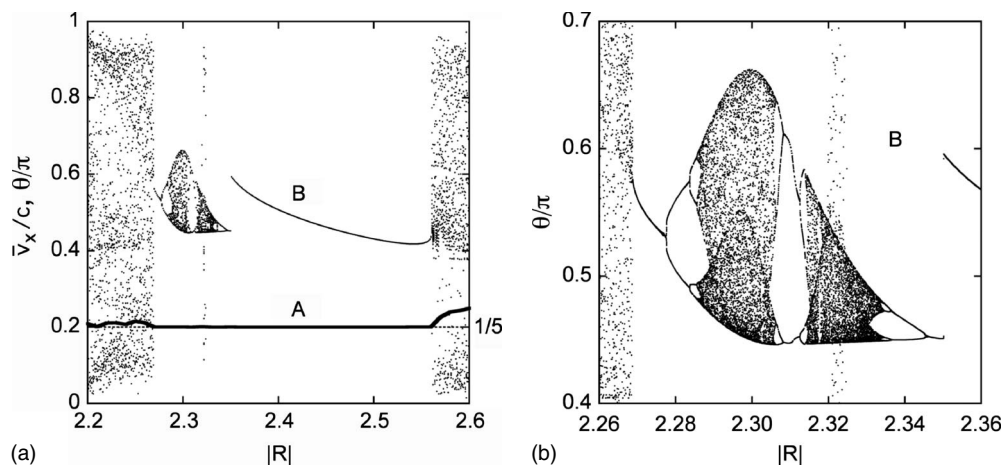
FIG. 8. (a) Velocity and contact-angle detail for the velocity 1/5 plateau of Fig. 7. (b) Contact angle detail near $R=2.3$ showing four period-doubling cascades to chaos, the first for increasing R near $R=2.28$, the second for decreasing R near $R=2.31$, the third for increasing R near $R=2.31$, and the fourth for decreasing R near $R=2.34$. Whereas only narrowband chaos is found between the first two cascades, a window of broadband chaos occurs above $R=2.32$ between the third and fourth. The transition from periodicity to broadband chaos below $R=2.27$ is abrupt.
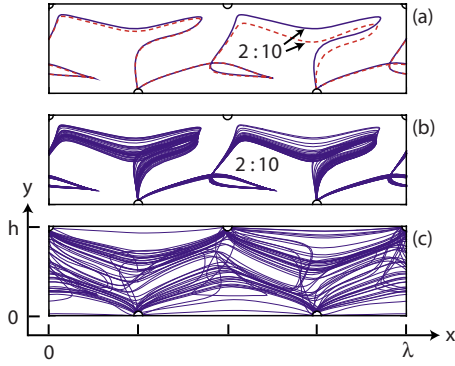
FIG. 9. (Color online) (a) Velocity-1/5 periodic attractors for $R=2.35$ (solid) and 2.34 (dashed). These attractors are associated with the fourth period-doubling cascade in Fig. 8(b) and involve only 2:10 interelectrode orbits. (b) Velocity-1/5 narrowband chaotic attractor for $R=2.33$ involving only 2:10 orbits. (c) Velocity-0.6836 broadband chaotic attractor for $R=3.2$ involving a variety of orbits.

be remarkably intricate. We have also studied (but do not include here) similar broadband attractors for other values of R. Most of the attractors in the partially trapped range $R_l < R < R_t$ of Fig. 7 appear to be broadband attractors, distinguished by widely scattered values of the contact angle and by velocities that are incommensurate with the wave speed. Transitions to such broadband attractors are abrupt, as seen at $R=R_t$ in Fig. 7, at $R=2.27$ and $R=2.56$ in Fig. 8, and at $R=1.93$ in Fig. 11.

In contrast with the narrowband attractor of Figs. 9(b) and 10(a), which samples a narrow range of electrode contact angles and involves a single interelectrode orbit ratio 2:10, the broadband attractor at $R=3.2$ samples the entire range of angles $0<\theta<\pi$ and employs a variety of interelectrode orbit ratios, as seen in Figs. 9(c) and 10(b). These orbits, combined in seemingly random ways, conspire to produce an incommensurate average velocity of 0.6836. Two of these orbits (2:2 and 4:4) are labeled in Fig. 10(b), from which it is difficult to determine the small-angle structure of the attractor. For this reason, we henceforth employ return maps of the extended contact angle

$$\theta'_{n+1} = \theta_{n+1} + \pi\Delta i \qquad (26)$$

as a function of the previous contact angle θ_n. For an interelectrode orbit with initial and final contact angles θ_n and θ_{n+1}, the extended contact angle θ'_{n+1} adds π to the contact angle θ_{n+1} for each electrode traveled in the $+x$ direction during this orbit. The number of such electrodes is Δi, the axial ion displacement measured in quarter wavelengths, as before [see Eq. (22)]. For example, $\Delta i=2$ for a $\Delta i:\Delta j=2:6$ orbit, giving $\theta'_{n+1}=\theta_{n+1}+2\pi$.

Figure 12 is an extended return map for the $R=3.2$ attractor that contains the same information as Fig. 10(b), except that Fig. 12(a) contains displacement information through the extended contact angle θ'_{n+1}. The extended format helps to illuminate the small-angle details, revealing an infinite sequence of singular angles θ^k, for $k=1,2,\ldots,\infty$, that approaches a singular accumulation angle $\theta^\infty=0.273775304\pi$. This accumulation angle and each of these singular angles correspond to a trapped orbit that travels indefinitely through the channel without contacting any electrodes. Also shown in Fig. 12 is an infinite sequence of step-transition angles θ_k^∞ that approaches this accumulation angle from above. Figure 12(c) shows fine detail at the accumulation point that certifies the robustness of our simulation code and the sharpness of the accumulation point. Clearly, for this chaotic attractor, the orbital behavior of an ion depends strongly on its angle of contact θ_n at the first electrode, which does not match the angle of arrival θ_{n+1} at the second electrode.

Distinct traces in Fig. 12 correspond to various interelectrode orbits that are sampled by the attractor, some of which are labeled on the figure. The step-transition angles θ_k^∞ mark the boundaries between trapped $2k:2k$ orbits, for $k=1,2,\ldots,\infty$. The singular angles θ^k separate complexes of partially trapped orbits that include the orbits $(k-2):(k+2)$, also for $k=1,2,\ldots,\infty$. These orbits are illustrated in Fig. 13: Ions depart from an electrode of origin (electrode 0, closed half-disk) and either return to this electrode or arrive at another electrode (open half-disk), moving Δi electrodes to the right in a time Δj measured in quarter periods for an orbit denoted
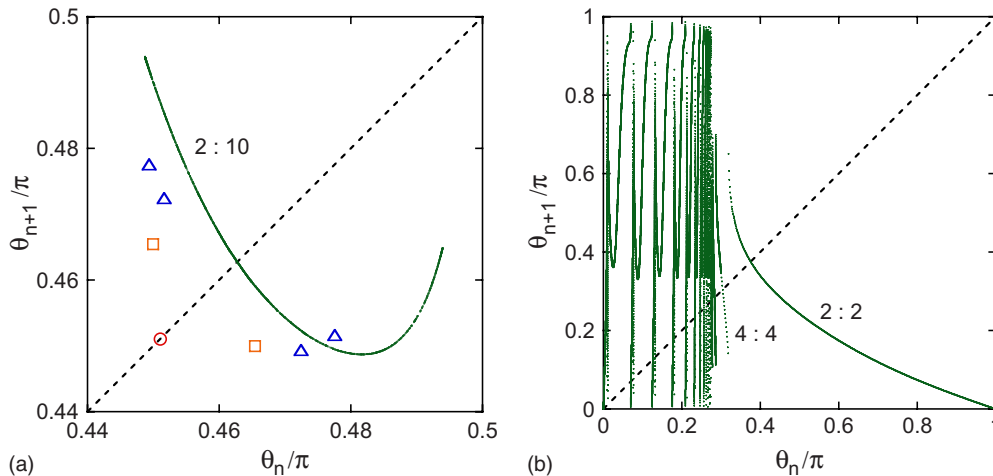
FIG. 10. (Color online) (a) Contact angle return maps associated with the attractors of Figs. 9(a) and 9(b) including a period-1 attractor (circle, $R=2.35$), a period-2 attractor (squares, $R=2.34$), a period-4 attractor (triangles, $R=2.335$), and a narrowband chaotic attractor (solid trace, $R=2.33$). (b) Return map for the broadband chaotic attractor (solid trace, $R=3.2$) of Fig. 9(c).
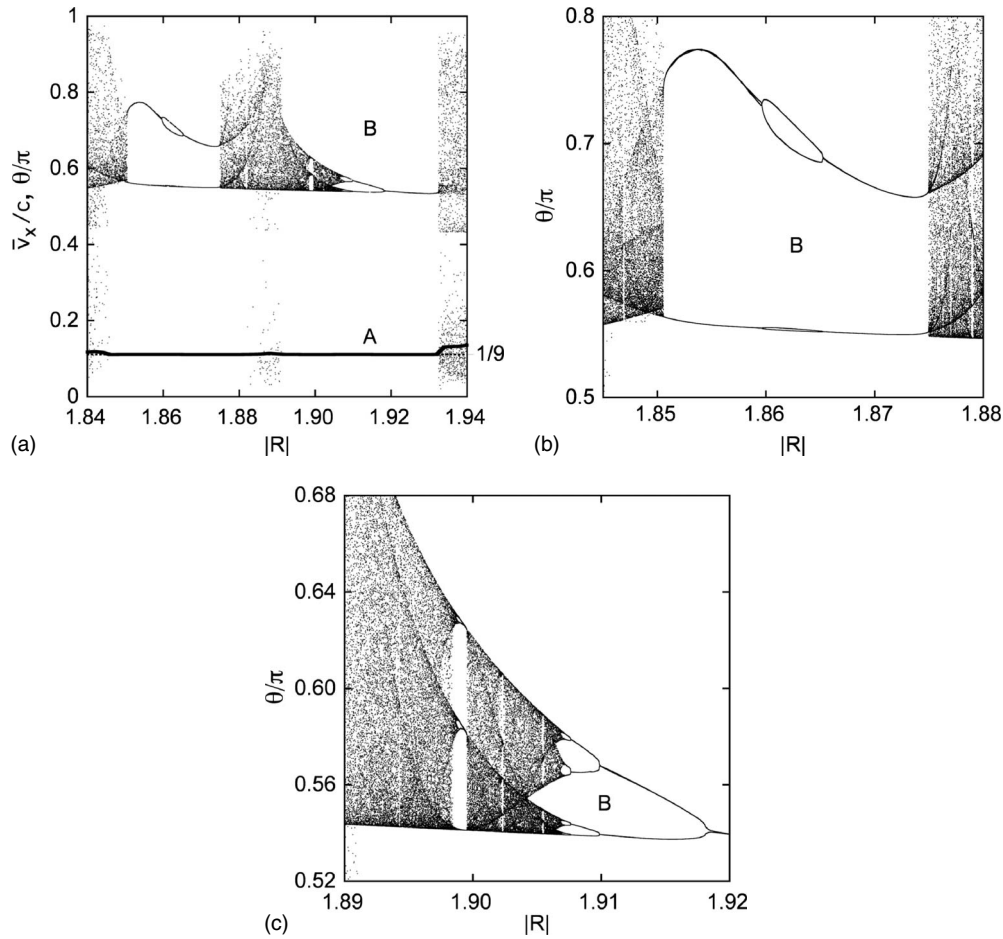
FIG. 11. (a) Velocity (a) and contact-angle (b) detail for the velocity-1/9 plateau from Fig. 7, showing periodic attractors (at $R=1.86$, for example) and narrowband chaotic attractors (at $R=1.88$, for example) associated with commensurate velocities $\bar{v}_x/c=1/9$ and broadband attractors (at $R=1.94$, for example) with incommensurate velocities. (b) The left side of the plateau features a period 2 attractor that bifurcates, near $R=1.86$, to a period 4 attractor, and back again. (c) The right side of the plateau features a classic period-doubling cascade.

by $\Delta i:\Delta j$. An orbit beginning at the accumulation angle θ^∞ is similar to the 6:6 orbit shown, but travels through the infinite channel without contacting any electrodes. The partially trapped orbits $(k-2):(k+2)$ travel $k-2$ quarter wavelengths axially with one lag cycle [see Eq. (22)] and include a retrograde $-1:3$ orbit for $k=1$ that moves one electrode to the left, a localized 0:4 orbit for $k=2$ that returns to the same electrode, and prograde orbits for $k \geq 3$ that move $k-2$ electrodes to the right.

The details of the θ^1 and θ^2 peaks of Fig. 12 are magnified in Fig. 14(a), which shows sequences of step transitions associated with each peak. The sequences for both peaks involve the same orbit ratios, 1:5, 2:6, 3:7, etc. Figure 13(c) shows how orbits having the same orbit ratios but pertaining to different peaks have fundamentally different trajectories. After departing from electrode 0, the 1:5 orbit associated with the θ^1 peak [leftmost orbit in Fig. 13(c)] is attracted successively to electrodes -2, -1, and 1, while the 1:5 orbit associated with the θ^2 peak [rightmost orbit in Fig. 13(c)], owing to its larger angle of departure from electrode 0, is attracted successively to electrodes 1, -1, and 1. Both of these are distinct from the 1:5 orbit near θ^3 that is labeled in Fig. 12(a). This orbit is attracted successively to electrodes 1,

2, and 1 [Fig. 13(b)]. Thus, orbits with the same orbit ratios that are associated with different segments on the return map [the 1:5 segments associated with the θ^1 and θ^2 peaks of Fig. 14(a), for example] take distinct paths to accomplish the same net displacement in the same amount of time. Trajectories that are associated with the same segment, such as trajectories for different values of θ within the 1:5 segment near θ^2, have only minor incremental differences.

Each singular-angle θ^k harbors remarkable substructure. For example, Fig. 14(b) magnifies the θ^1 peak horizontally to show how it splits into a doublet, θ^{1-} and θ^{1+}, of separation $\theta^{1+}-\theta^{1-}=1.2\times10^{-4}\pi=7.9$ min of arc. This figure also shows how a descending sequence of step transitions θ_k^{1+} between the odd orbits $-1:3$, 1:5, 3:7, ... approaches θ^{1+} from above, while an ascending sequence of step transitions θ_k^{1-} between the even orbits 0:4,2:6,4:8,... approaches θ^{1-} from below. Figure 14(c) magnifies the doublet $\theta^{1\pm}$ yet further, revealing infinite ascending and descending sequences of singular angles *within* the doublet.

Figure 15(a) shows the details of the ascending sequence of singular angles $\theta^{1+,k}$ that leads to θ^{1+}, for $k=1,2,3,\ldots,\infty$. Figure 15(a) is similar to Fig. 12. Both feature an accumulation angle that is approached from below by a sequence of
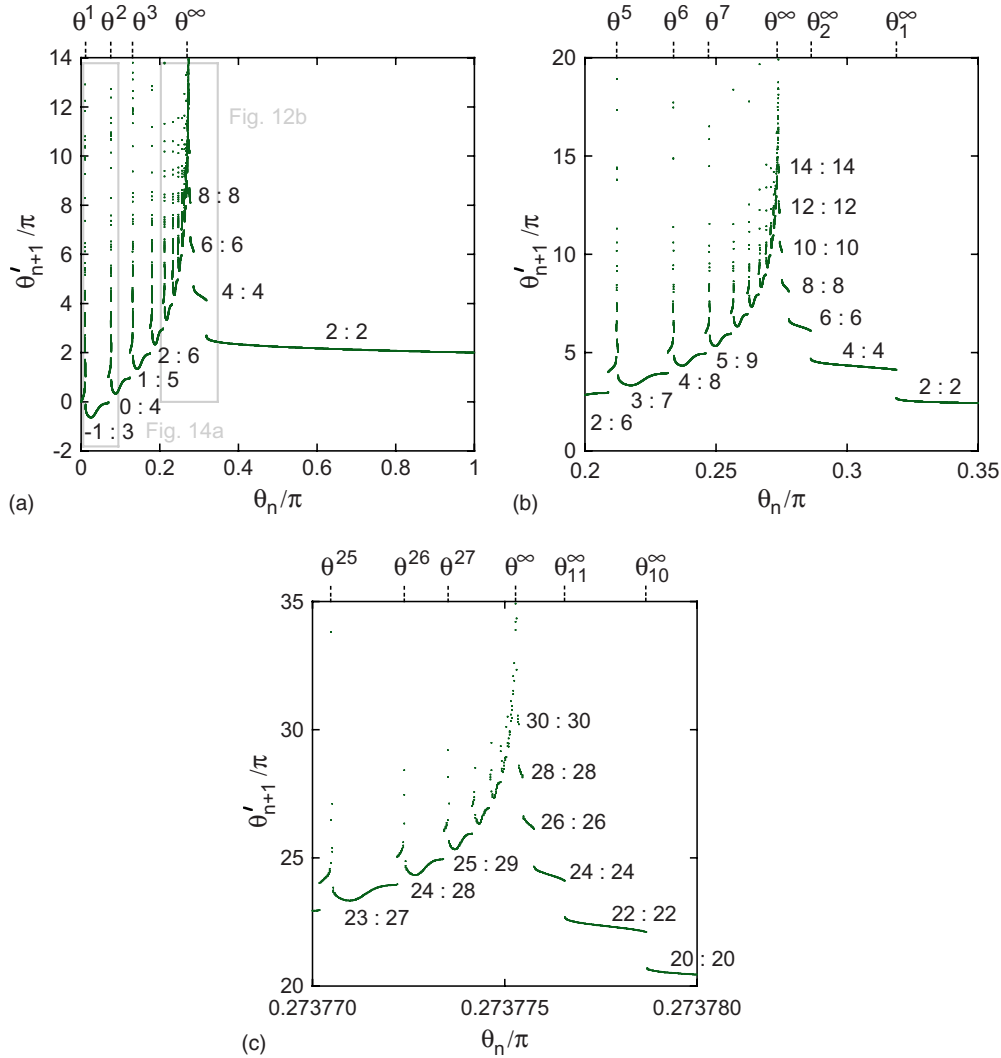
FIG. 12. (Color online) Extended contact-angle return map for a broadband chaotic attractor with $R=3.2$ [Figs. 9(c) and 10(b)] showing the approach to a singular accumulation angle θ^∞ via an ascending sequence of singular angles θ^k (labeled), with $k=1,2,\ldots,\infty$, and the approach to the same angle via a descending sequence of step-transition angles θ_k^∞. Frames (a)–(c) show increasing detail near θ^∞. Gray rectangles identify regions that are shown in greater detail elsewhere.

singular angles and is approached from above by a sequence of step transitions.

Figure 15(b) magnifies the peak at $\theta^{1+,1}$ of Fig. 15(a), showing how this peak splits into a doublet, $\theta^{1+,1-}$ and $\theta^{1+,1+}$, of separation $\theta^{1+,1+}-\theta^{1+,1-}=5.6\times10^{-8}\pi=0.036$ s of arc, enclosing a sequence of singular angles. Figure 15(b) is similar to Fig. 14(c). Both feature a doublet that encloses an apparently infinite sequence of singular angles and that is enclosed by sequences of step transitions.

We now investigate the convergence of sequences that populate the $R=3.2$ attractor. A log-linear plot of the singular-angle margins $\Delta\theta^k=\theta^\infty-\theta^{k+}$ vs. k (Fig. 16, circles A) suggests geometric convergence of the singular angles θ^{k+} to the accumulation angle as θ^∞ $k\to\infty$ according to

$$\Delta\theta^k \to A\alpha^{-k}, \tag{27}$$

where A and α are constants. Indeed, a linear fit to the nine data points with the largest values of k ($k=29$ through k

$=37$, trace A of Fig. 16) yields the convergence factor

$$\alpha = 1.647 \pm 0.002 \tag{28}$$

for the sequence. This fit incorporates uncertainties in $\Delta\theta^k$ of $1\times10^{-9}\pi$, which are smaller than the plotting symbols. The value $\chi^2=0.79$ of the fit merit function and the value $Q=0.998$ of the goodness-of-fit parameter [32] confirm that the fitted data obey Eq. (27). Thus we conclude that θ^{k+} converges geometrically to θ^∞ as $k\to\infty$, though the value $\alpha=1.647\pm0.002$ was computed for finite k and might therefore underestimate the asymptotic result for $k\to\infty$.

Fits to $\Delta\theta^k$ that include points with smaller values of k have unacceptably large values of χ^2, indicating that the small-k data depart significantly from the scaling law of Eq. (27). Fits to fewer than nine large-k data points yield acceptable values of χ^2 and yield values of α that agree with Eq. (28), but with larger uncertainties. Thus, the nine fit points
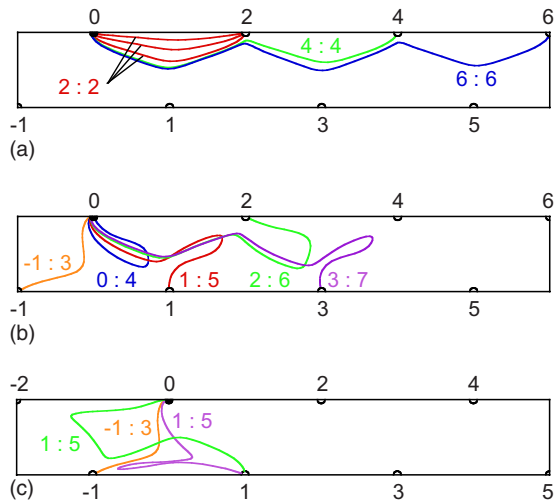
FIG. 13. (Color online) Interelectrode orbits that contribute to the broadband chaotic attractor for $R=3.2$ [see Figs. 9(c) and 12]. The closed half-disk represents electrode 0, the electrode of origin. (a) Trapped orbits associated with a descending sequence of step transitions, showing three 2:2 orbits that depart from the electrode of origin at the contact angles $\theta/\pi=0.8$, 0.6, and 0.4, one 4:4 orbit for $\theta/\pi=0.3$, and one 6:6 orbit for $\theta/\pi=0.28$. (b) Untrapped -1:3, 0:4, 1:5, 2:6, and 3:7 orbits that participate in an ascending sequence of singular angles, with $\theta/\pi=0.05$, 0.1, 0.15, 0.2, and 0.22. (c) Two 1:5 orbits, for $\theta/\pi=0.0105$ and 0.071, flanking the -1:3 orbit at $\theta/\pi=0.05$ in Fig. 14(a). These 1:5 orbits are distinct from each other and from the 1:5 orbit shown in (b).

represents the largest acceptable number of fitted points consistent with Eq. (27).

Figure 16 includes the doublet separations $\Delta\theta^{k'}=\theta^{k+}-\theta^{k-}$ (circles B) and the level-2 singular-angle margins $\Delta\theta^{k''}=\theta^{\infty}-\theta^{1+,k+}$ (circles C). Linear fits with $\alpha=1.647$ (traces B and C) evidently capture the $k\to\infty$ behavior of these data and suggest geometric convergence according to Eqs. (27) and (28) for all sequences of singular angles.

Figure 16 also includes the margins $\Delta\theta_k=\theta_k^{\infty}-\theta^{\infty}$ (squares D) associated with the step-transition sequence that culminates at θ^{∞} and the margins $\Delta\theta_k'=\theta_k^{1+}-\theta^{1+}$ (squares E) associated with the level-2 step-transition sequence that culminates at θ^{1+}. These step-transition data clearly differ in slope from the singular-angle sequences (circles A, B, and C), suggesting convergence as $k\to\infty$ with a difference convergence factor than Eq. (27) according to

$$\Delta\theta_k \to B\beta^{-k}, \tag{29}$$

where B and β are constants. Indeed, for $\Delta\theta_k=\theta_k^{\infty}-\theta^{\infty}$, a linear fit to the six data points with the largest values of k ($k=10$ through $k=15$, trace D) yields the convergence factor

$$\beta = 2.7097 \pm 0.0004 \tag{30}$$

for the sequence. The associated values $\chi^2=0.31$ and $Q=0.989$ confirm that the fitted data obey Eq. (29) and that θ_k^{∞} converges geometrically to θ^{∞} as $k\to\infty$. A fit to $\Delta\theta_k'$ (trace E) using the same value of β evidently captures the $k\to\infty$ behavior of $\Delta\theta_k'$ and suggests geometric convergence according

to Eqs. (27) and (28) for all sequences of step-transition angles.

VIII. DISCUSSION

A two-dimensional model of wave electrophoresis driven by a periodic array of synchronized electrodes yields a rich spectrum of dynamical behavior. The phase relationships between the electrode potentials demand average velocities that are commensurate with the wave speed (rational $\bar{v}_x/c$) and mode locking of the lag and wave frequencies (rational Ω/ω) for periodic and narrowband chaotic attractors, and incommensurate velocities for broadband chaotic orbits.

The contact-angle return maps $\theta_{n+1}=f(\theta_n)$ in our 2D nonautonomous system are true 1D iterated maps because the time of departure from an electrode is prescribed by the applied external potential, and because the time of arrival and the angle of contact at a second electrode are determined uniquely by the contact angle at the first electrode. Consequently, even our return maps for broadband chaotic attractors are single-valued functions. The Lorenz map, which gives the heights of successive peaks in a 3D autonomous chaotic attractor, has a tent shape of finite thickness and is therefore not single valued [33]. Since our return maps are single-valued functions, standard cobwebbing and fixed-point techniques may be used to study our attractors [30,34].

The return maps of our broadband chaotic attractors possess fascinating self-similar structure, including infinite numbers of nested infinite sequences of singular angles characterized for $R=3.2$ by the geometric convergence factor $\alpha=1.647\pm0.002$, and infinite numbers of nested infinite sequences of step-transition angles characterized for $R=3.2$ by a different convergence factor $\beta=2.7097\pm0.0004$. Our simulations of broadband attractors with other values of R identify similar behavior, but with different convergence factors. We are not aware of other examples of a chaotic return map with self-similar nested geometric sequences [Figs. 10(b), 12, and 14–16] in the literature.

Equation (27) implies that α may be estimated from a triad of adjacent values of θ^k as $k\to\infty$ according to

$$\alpha \to \frac{\theta^k - \theta^{k-1}}{\theta^{k+1} - \theta^k}, \tag{31}$$

and that β may be estimated in a similar way using values of θ_k^{∞}. Equation (31) is the well-known Feigenbaum result for period-doubling cascades, which are characterized by the convergence factors $\delta=4.669$, the Feigenbaum constant, and $\alpha=2.503$, the reduction parameter [30,31]. Feigenbaum's sequences refer to bifurcations between periodic attractors as some control parameter is varied, while our sequences refer to orbits that are sampled by a single broadband chaotic attractor at a particular value of the control parameter ($R=3.2$, for example).

Although measurement of contact angles might be impractical in a microfluidic environment, some details of orbits and velocities should be observable, and might help to evaluate the theory as a tool for designing microfluidic separation systems. Previous measurements of the velocity of a fluorescein plug for $\Gamma=5.3$ agree generally with trace C of
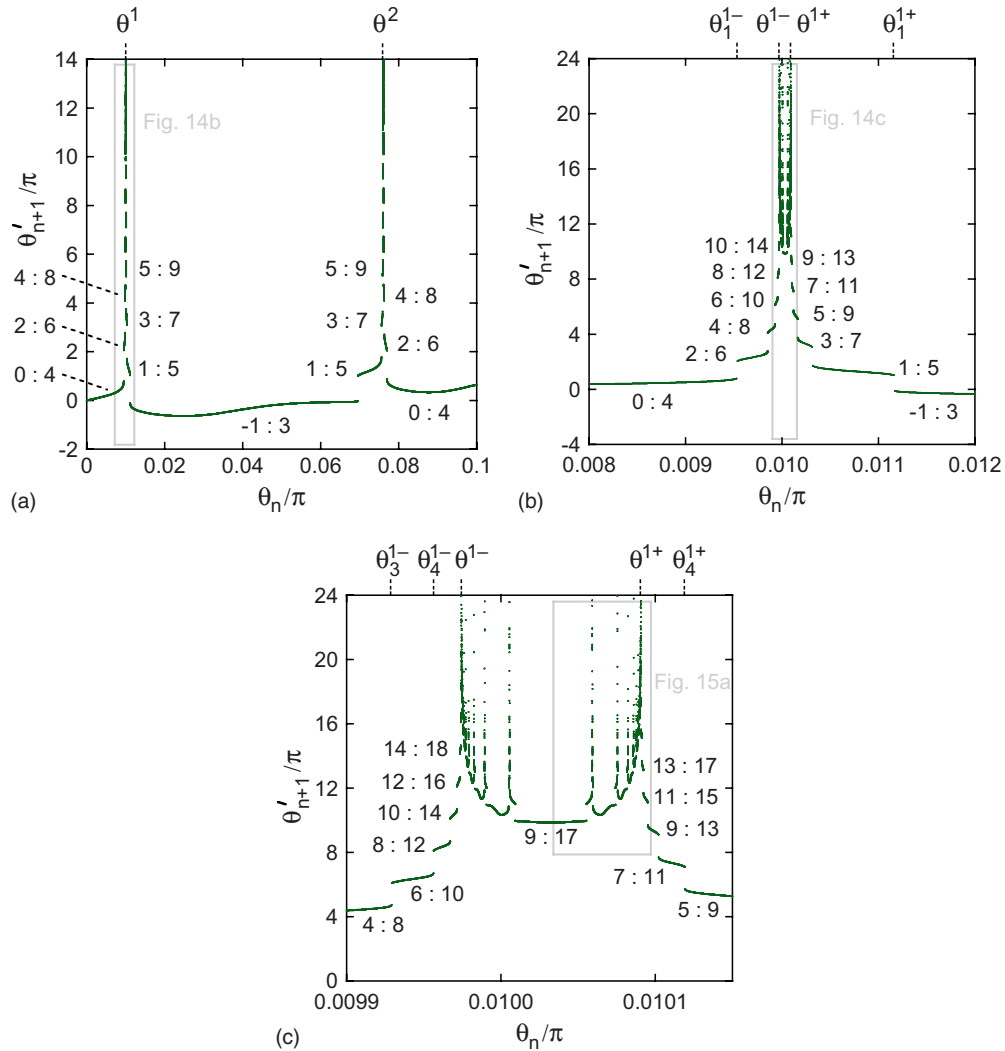
FIG. 14. (Color online) Small-angle details of Fig. 12(a) showing how the singular angle θ^1 resolves into a doublet of closely spaced accumulation angles θ^{1-} and θ^{1+} that enclose ascending and descending sequences of singular angles. Shown also are sequences of step-transition angles $\theta_k^{1\pm}$ that approach these angles, for $k=1,2,3,\ldots,\infty$.
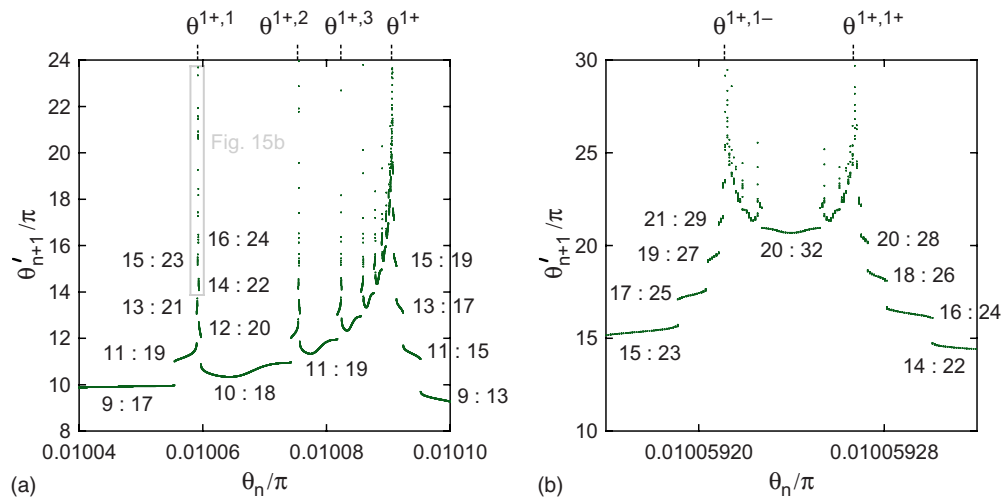
FIG. 15. (Color online) (a) Details of the ascending sequence of singular angles $\theta^{1+,k}$ that approach the accumulation angle θ^{1+} of Fig. 14(c), with $k=1,2,3,\ldots,\infty$. This sequence is similar to the sequence θ^k that approaches θ^∞, as shown in Fig. 12. (b) Fine detail near $\theta^{1+,1}$, which resolves into a doublet of closely spaced accumulation angles $\theta^{1+,1-}$ and $\theta^{1+,1+}$ that enclose ascending and descending sequences of singular angles similar to Fig. 14(c).
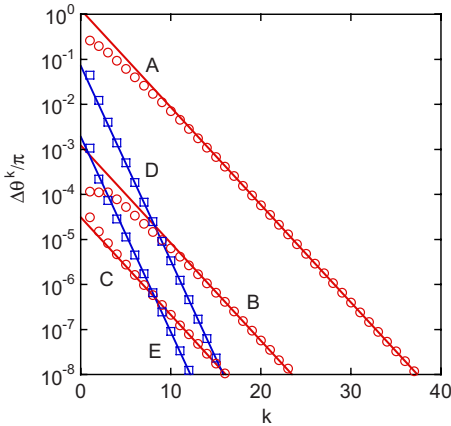
FIG. 16. (Color online). Log-linear plot of singular-angle margins $\Delta\theta^k = \theta^\infty - \theta^{k+}$ [circles A, see Fig. 12(a)], doublet separations $\Delta\theta^{k'} = \theta^{k+} - \theta^{k-}$ [circles B, see Fig. 14(b)], and level-2 singular-angle margins $\Delta\theta^{k''} = \theta^\infty - \theta^{1+,k+}$ [circles C, see Fig. 15(a)] vs k, all of which vanish geometrically as $k \to \infty$ according to Eqs. (27) and (28) (traces A, B, and C). Also shown are step-transition margins $\Delta\theta_k = \theta_k^\infty - \theta^\infty$ [squares D, see Fig. 12(b)] and the level-2 step-transition margins $\Delta\theta_k' = \theta_k^{1+} - \theta^{1+}$ [squares E, see Figs. 14(b) and 14(c)] vs k, both of which vanish geometrically as $k \to \infty$ according to Eqs. (29) and (30) (traces D and E).

Fig. 4 [9] but fail to resolve the finer details, including the velocity plateaus. If molecular diffusion is responsible for this failure, then measurements with small concentrations of charged fluorescent beads or quantum dots should increase the resolution of the velocity details. Using confocal fluorescence microscopy, my experimental collaborators, Lloyd Carroll and Aaron Timperman, plan to use low concentrations of semiconductor quantum dots and ultrasmall fluores-

cent microspheres to image the 2D and 3D motions of particles with varying mobilities under the influence of the traveling wave. These experiments, while challenging, are possible, and will provide experimental determination of the paths taken by particles as they move through the channel. Such measurements could provide feedback needed to refine and extend our models.

Traveling-wave electrophoresis holds promise for particle separations. In contrast with stochastic resonance separations [35], capillary electrophoresis and traveling-wave electrophoresis apply only to species of different mobilities. Capillary electrophoresis [36] can be used to separate species whose mobilities differ by much less than 1%. A complete evaluation of the sensitivity of traveling-wave electrophoresis awaits the inclusion of molecular diffusion in the theory and experiments involving multiple species, which are underway. In contrast with capillary electrophoresis and stochastic resonance, traveling-wave electrophoresis offers separation thresholds R_t and R_l (Sec. V) that can be tuned to particular species using Eq. (3) simply by varying the amplitude or frequency of the electrode potentials. Figure 4 shows that these thresholds are very sharp in many instances, indicating promise for very sensitive separations.

[1] E. N. Lorenz, J. Atmos. Sci. **20**, 130 (1963); see also **63**, 2056 (2006).

[2] S. Kadar, J. Wang, and K. Showalter, Nature (London) **391**, 770 (1998).

[3] J. Wang, S. Kadar, P. Jung, and K. Showalter, Phys. Rev. Lett. **82**, 855 (1999).

[4] O. U. Kheowan, E. Mihaliuk, B. Blasius, I. Sendina-Nadal, and K. Showalter, Phys. Rev. Lett. **98**, 074101 (2007).

[5] F. Rogister and R. Roy, Phys. Rev. Lett. **98**, 104101 (2007).

[6] Y. Braiman, J. F. Lindner, and W. L. Ditto, Nature (London) **378**, 465 (1995).

[7] M. E. Koepke, A. Kinklage, T. Klinger, and C. Wilke, Phys. Plasmas **8**, 1432 (2001); K.-D. Weltmann, M. E. Koepke, and C. A. Selcher, Phys. Rev. E **62**, 2773 (2000); T. Klinger, F. Greiner, A. Rohde, A. Piel, and M. E. Koepke, *ibid.* **52**, 4316 (1995).

[8] A. Pikovsky, M. Rosenblum, and J. Kurths, *Synchronization: A Universal Concept in Nonlinear Sciences* (Cambridge, New York, 2003).

[9] B. F. Edwards, A. T. Timperman, R. L. Carroll, K. Jo, J. M. Mease, and J. E. Schiffbauer, Phys. Rev. Lett. **102**, 076103

(2009).

[10] S. Masuda, M. Washizu, and M. Iwadare, IEEE Trans. Ind. Appl. **IA-23**, 474 (1987); S. Masuda, M. Washizu, and I. Kawabata, *ibid.* **24**, 217 (1988).

[11] H. Kawamoto and S. Hayashi, J. Phys. D **39**, 418 (2006); H. Kawamoto, K. Seki, and N. Kuromiya, *ibid.* **39**, 1249 (2006), and references therein.

[12] M. H. Lean, H. B. Hsieh, A. R. Volkel, in *IEEE/EMBS Proceedings Conference on Microtechnologies in Medicine and Biology* (IEEE, 2005), p. 356; M. H. Lean, A. R. Volkel, H. B. Hsieh, J.-P. Lu, J. H. Daniel, B. T. Preas, and S. J. Limb, in *IEEE/EMBS Proceedings Conference on Microtechnologies in Medicine and Biology*, (IEEE, 2005), p. 80.

[13] A. Ramos, H. Morgan, N. G. Green, A. Gonzalez, and A. Castellanos, J. Appl. Phys. **97**, 084906 (2005).

[14] R. M. Ehrlich and J. R. Melcher, Phys. Fluids **25**, 1785 (1982).

[15] R. D. Astumian, Science **276**, 917 (1997).

[16] H. Du, W. H. Li, D. F. Chen, and C. Shu, Int. J. Mech. Mater. Des. **1**, 115 (2004).

[17] Y. L. Li, C. Dalton, H. J. Crabtree, G. Nilsson, and K. V. I. S.

Kaler, Lab Chip **7**, 239 (2007).

[18] H. Nyquist, Trans. AIEE **47**, 617 (1928); reprint as a classic paper in Proc. IEEE **90**, 280 (2002).

[19] C. E. Shannon, Proc. IRE **37**, 10 (1949); reprint as classic paper in Proc. IEEE **86**, 447 (1998).

[20] C. B. Wharton, J. H. Malmberg, and T. M. O-Neil, Phys. Fluids **11**, 1761 (1968).

[21] R. N. Franklin, S. M. Hamberger, H. Ikezi, G. Lampis, and G. J. Smith, Phys. Rev. Lett. **28**, 1114 (1972).

[22] H. X. Vu, D. F. DuBois, and B. Bezzerides, Phys. Rev. Lett. **86**, 4306 (2001).

[23] S. H. Strogatz, *Nonlinear Dynamics and Chaos* (Addison-Wesley, New York, 1994), Sec. 1.2.

[24] N. A. Magnitskii and S. V. Sidorov, Differ. Eq. **42**, 1579 (2006).

[25] J. R. Melcher, E. P. Warren, and R. H. Kotwal, Part. Sci. Technol. **7**, 1 (1989).

[26] H.-H. Wei, Appl. Phys. Lett. **90**, 204103 (2007).

[27] R. K. Wangsness, *Electromagnetic Fields* (Wiley, New York, 1986), Sec. 5–3.

[28] W. H. Press, S. A. Teukolsky, W. T. Vetterling, and B. P. Flannery, *Numerical Recipes in C++* (Cambridge University Press, New York, 1992), function odeint, Sec. 16.2.

[29] J. Maselko and H. L. Swinney J. Chem. Phys. **85**, 6430 (1986).

[30] R. M. May, Nature (London) **261**, 459 (1976).

[31] M. J. Feigenbaum, J. Stat. Phys. **19**, 25 (1978).

[32] W. H. Press, S. A. Teukolsky, W. T. Vetterling, and B. P. Flannery, *Numerical Recipes in C++* (Cambridge University Press, New York, 1992), function odeint, Ch. 15.

[33] S. H. Strogatz, *Nonlinear Dynamics and Chaos* (Addison-Wesley, New York, 1994), Sec. 9.4.

[34] S. H. Strogatz, *Nonlinear Dynamics and Chaos* (Addison-Wesley, New York, 1994), Sec. 10.1.

[35] D. Alcor, V. Croquette, L. Jullien, and A. Lemarchand, Proc. Natl. Acad. Sci. U.S.A. **101**, 8276 (2004).

[36] J. W. Jorgenson and K. D. Lukacs, Science **222**, 266 (1983).